Sociedad Mexicana de Ingeniería Mecánica
Fecha de recepción: 03-09-2018
Fecha de aceptación: 07-06-2019

INGENIERÍA MECÁNICA
TECNOLOGÍA Y DESARROLLO
Vol. 6 No. 5 (2019) 169 - 184

Drag forces on a semisubmersible platform column for different corners curvature radius

Fuerzas de arrastre en una columna de plataforma Semisumergible para diferentes radios de curvatura en las esquinas

J. Sanchez-Mondragon[a], Oscar A. Godoy-Marroquin[b], A.R. Cruces-Giron[b], Ivan Felix-Gonzalez[b*]
[a]CONACYT-Instituto Mexicano del Petróleo, Eje Central Lázaro Cárdenas 152, Gustavo Madero 07730, México D. F., México.
[b]Instituto Mexicano del Petróleo, Eje Central Lázaro Cárdenas 152, Gustavo A. Madero 07730, México D. F., México.
*Corresponding autor: ifelix@imp.mx

Abstract

In an early design stage of a floating production system, the definition of certain important characteristics are required, such as production or storage capacities, and others related to the strength of the floating system hull against waves, wind and current forces. Based on these, the dimensions of the platform are derived, and in the particular case of semi-submersible platforms and tensioned leg platforms the dimensions of their columns, as well as the curvature radius of the column corner. This work focuses on the calculation of marine current drag forces on a large dimension column (17.2 m width) considering a range of curvature radius on corners. Reducing marine current forces is a very important issue in floating oil production platforms with large dimensions columns (as semisubmersibles or tension leg platforms). In order to capture turbulence effects three-dimensional Reynolds-Averaged Navier-Stokes (RANS) simulations are developed using k-ω Shear Stress Transport (SST) viscous model. Even for small current velocities, high Reynolds numbers are presented due to the large column dimensions. Results show that drag forces has a fast decay for radius from 1 m to 1.5 m, for greater radius drag forces presents small changes. Additionally, flux behavior is analyzed; the associated vertical flux that modifies the horizontal behavior about the vertical level and the flux trace behavior in function of Reynolds number.

Resumen

En las primeras etapas de diseño de un sistema flotante de producción se requiere la definición de ciertas características importantes como son capacidades de producción o almacenamiento, otras corresponden a la resistencia del sistema flotante ante fuerzas de oleaje, viento y corriente, de estas se derivan las dimensiones de la plataforma, y en el caso particular de plataformas semisumergibles y plataformas de piernas tensionadas las dimensiones de sus columnas, así como la curvatura de las mismas. Este trabajo se enfoca en el cálculo de fuerzas de arrastre debidas a la corriente marina en una columna de gran dimensión (17.2 m de ancho) considerando un rango de radios de curvatura en las esquinas de la misma. La reducción de las fuerzas actuantes es un tema importante para el diseño de sistemas flotantes de producción de petróleo con columnas de grandes dimensiones. Para capturar los efectos de la turbulencia, se desarrollan simulaciones tridimensionales empleando las ecuaciones de Navier-Stokes promediadas por Reynolds (RANS) utilizando el modelo de turbulencia de transporte de esfuerzo cortante k-ω (SST). Incluso para velocidades de corriente pequeñas, se presentan números de Reynolds elevados debido a las grandes dimensiones de la columna. Los resultados muestran que las fuerzas de arrastre tienen un rápido decaimiento para un radio de curvatura en las esquinas de 1 m a 1.5 m, para radios de curvatura mayores se presentan pequeños cambios en las fuerzas de arrastre. Además, se analiza el comportamiento del flujo; así como el efecto del flujo vertical que modifica el comportamiento horizontal en los niveles verticales y el patrón de flujo en función del número de Reynolds.

ISSN 2448-5837

Edición digital

Keywords:
CFD analysis, Drag coefficient, Offshore structure, Column with square transverse section, High Reynolds number

Palabras clave:
análisis de CFD, Coeficientes de Arrastre, Estructuras costa afuera, Columnas con sección transversal cuadrada, Números de Reynolds alto

Nomenclature

A_{size}	Mesh size in the domain-A, ***m***
A_y	Projected area normal to the inlet velocity, ***m²***
B_{size}	Mesh size in the domain-B, ***m***
Cd	Drag coefficient; $\frac{F_y}{\frac{1}{2}\rho v^2 A_y}$
Cd_{MI}	Drag coefficient for MI mesh resolution
Cd_{MII}	Drag coefficient for MII mesh resolution
Cd_{MIII}	Drag coefficient for MIII mesh resolution
C_{size}	Mesh size in the domain-C, ***m***
D	Square transversal section, ***m***
D_ω	Cross-diffusion term, $\boldsymbol{kg/m^3\,s^2}$

F_y	Stream wise, $\boldsymbol{kg\,m/s^2}$
$\tilde{G}_k$	Generation of turbulence by kinetic energy, $\boldsymbol{kg\,m/s^3}$
$\tilde{G}_\omega$	Generation of ω, $\boldsymbol{kg/m^3s^2}$
MI	Mesh resolution configuration, **0.3*m*\0.6*m*\2.4*m***
MII	Mesh resolution configuration, **0.4*m*\0.8*m*\3.2*m***
$MIII$	Mesh resolution configuration, **0.5*m*\1.0*m*\4.0*m***
R	Rounded corner radius, ***m***
Re	Reynolds number; $\boldsymbol{UD\rho/\mu}$
U	Uniform velocity, ***m/s***
$Xfxp$	Reference plane defined at the middle of the column and normal to the x-axis

Yfxp	Reference plane defined at 10*m* from the backward end of the column and normal to the *y* axis
$\mathbf{Zfxp_1}$	Reference plane defined at 10*m* above the lower end of the column and normal to the *z* -axis
$\mathbf{Zfxp_2}$	Reference plane defined at 20*m* above the lower end of the column and normal to the *z*-axis
$\vec{U}=(u, v, w)$	Vector flow velocity and its cartesian components, **(*m/s,m/s,m/s*)**
U_c	Velocity condition on the column, ***m/s***
Y_k	Diffusivity by turbulence of *k*, $\mathbf{kg/ms^3}$
Y_ω	Diffusivity by turbulence of *ω*, $\mathbf{kg/m^3\,s^2}$
k	Turbulent kinetic energy, $\mathbf{m^2/s^2}$
p	Dynamic pressure, ***Pa***
u_i	Mean velocities, ***m/s***
u'_i	Fluctuating part of the velocity, ***m/s***
v	Velocity from the inlet flow, m/s
Δ_{II-I}	Relative change between Cd_{MII} and Cd_{MI} drag coefficients, %
Δ_{III-I}	Relative change between Cd_{MIII} and Cd_{MI} drag coefficients, %
δ_{ij}	Kronecker delta
μ	Dynamic viscosity, ***kg/ms***
μ_t	Turbulent viscosity, ***kg/m***
ρ	Fluid density, $\mathbf{kg/m^3}$
σ_k	Constant for ***k***
σ_ω	Constant for ***ω***
ω	Dissipation rate, ***1/s***

Introduction

The worldwide oil industry is moving to develop fields in deeper water which is a technological and engineering challenge, Semi-Submersible Platform (SSP) are commonly used to exploit those fields. SSP responses are influenced by environmental loads (i.e. waves, marine currents and winds). The forces on the floating structures can be analyzed in separate ways, for example, the effects of waves can be calculated considering the radiation and diffraction of these, based on potential flow theory, which assumes that the fluid is inviscid and the flow is irrotational. Moreover, wind and marine currents forces are obtained based on experimental tests and advanced numerical simulations considering turbulence phenomena on the flow, as Computational Fluid Dynamics (CFD).

One of the structural engineering challenge is minimize the loads effects, in particular this research work is focused on assessing the loads effect on SSP due to marine currents. The SSP commonly have columns with square section and rounded corners. Also, in fluid mechanics, the flow around square cylinders is of great interest for a wide range of civil and offshore engineering applications. Many of these engineering applications are often subject to flow conditions corresponding to very high Reynolds numbers because their large dimensions, even at low current velocities, with typical values of $O(10^6)$-$O(10^7)$. At those Reynolds numbers, experimental studies are still a very challenging subject in hydrodynamics because most of the flow visualization techniques (smoke line, PIV, etc.) don't work well at high Reynolds number conditions due to the strong dissipation of the particles or smoke in air or water. Numerical techniques require high computational cost, however, they have become a common solution to overcome this problem.

Due to the nature of the study, the literature review is concentrated on works where high Reynolds numbers ($Re > 10^5$) are used. This covers the supercritical ($3.5\times10^5<Re<1.5\times10^6$) to transcritical ($Re > 4\times10^6$) flow regimes, where Reynolds number is defined as $Re=UD\rho/\mu$, where U is the uniform approach velocity, D is the square transversal section, ρ is the fluid density and μ is the fluid dynamic viscosity. Therefore, in what follows we present a theoretical frame works on 3D and 2D, square, rectangular and circular columns.

On square cylinders, the replacement of sharp corners by the introduction of chamfered or rounded corners alters the flow characteristics originating the reduction of drag forces [1] - [6]. For this reason, the replacement of sharp corners with rounded ones is one of the most widely adopted drag reduction techniques. Bearman et al. [1] investigated the corner radius effect on the hydrodynamic forces of cylindrical bluff bodies with square and diamond configurations for $Re=2.0\times10^2$-2.0×10^4 and found that the drag coefficient is sensitive to the corner curvature.

Okamoto and Uemura [2] investigated experimentally the effect of the corner radius on the flow past a cube at Reynolds number $Re=4.72\times10^4$, and found that the drag coefficient decreases rapidly in the corner ratio range of $0\leq R/D\leq0.15$. Moreover, Kawai [3] investigated experimentally the effects of corner shapes (corner cut and rounding on squares and rectangular prism) at $Re=3.4\times10^4$ and concluded that corner rounding is the best option to provide aerodynamic stability. Furthermore, Tamura *et al.* [4] studied three dimensional unsteady flow for chamfered and rounded corners at $Re=1.0\times10^4$-1.0×10^6 and discovered that these modifications could decrease the drag coefficients approximately by 60%. Finally, Miran and Shon [5] [6] studied the effect of corner radius on square cylinders first on stationary and then on oscillating cylinders for $Re=500$, and found that the Strouhal number has approximately the same value, but drag coefficients increased for oscillating cylinders. However, in both cases drag coefficients have minimum values for corner ratio (R/D) between 0.2 and 0.3.

Ong [7] used Unsteady Reynolds-Averaged Navier-Stokes (URANS) simulations with the k-ε viscous model for a 2D rectangular cylinder at $Re=5.0\times10^5$ to $Re=2.0\times10^6$ to evaluate time-averaged drag coefficient, root-mean-square lift coefficient, Strouhal number and mean pressure distributions, which was in accordance with published experimental data. Tian *et al.* [8] used URANS simulations with the k-ω-SST viscous model to simulate 2D rectangular cylinders with different aspect ratios for $Re=2.14\times10^4$ to determine drag forces and vortex shedding, and report that vortex shedding frequencies are not sensitive to the aspect ratio.

Sohankar [9] used the Large Eddy Simulation model (LES) to simulate flow effects between two square cylinders in 2D for *Re*=1.0×10^3 and *Re*=1.0×10^5. In his work was variated the gap-spacing between the cylinders from 1 to 12 times the width of the cylinders, to study the reduction of drag coefficient and found three major regimes according to the normalized gap spacing between cylinders.

Tong *et al*. [10] used *k-ω* model to calculate the drag coefficient values and showed a reduction on those values by corner chamfers on 2D square columns from *Re*=3.24×10^4 to *Re*=1.62×10^6 to contribute to an archival repository for drag coefficients information. Dai et al. [11] studied the flow over rounded corners on 2D square column at subcritical Reynolds number (*Re*=2.0×10^4-2.0×10^5) with standard and modified *k-ε* models and found that downstream rounded corners make separation point move backward and increase the base pressure behind the column.

On the canonical problem of flow over 2D circular cylinders, Wang *et al*. [12] used the LES model for high Reynolds numbers (*Re*=5.0×10^5, 1.0×10^6 and 2.0×10^6) which reduced drag coefficients are consistent with measurements after the drag crisis. Catalano *et al*. [13] compared the LES model with steady and unsteady Reynolds-Averaged Navier-Stokes simulations in the supercritical regime (*Re*=5.0×10^5, 1.0×10^6 and 2.0×10^6), and obtained accurate drag coefficient results for *Re*=5.0×10^5 and 1.0×10^6, however at *Re*=2.0×10^6 Reynolds number dependency was not captured.

Singh and Mittal [14] studied the relationship between sudden loss of drag at *Re*=2.0×10^5 (drag crisis) and the instability of the separated layer using the Generalized Minimal RESidual technique (GMRES), and found that the shear layer vortices play a major role in the transition of boundary layer from laminar to turbulent state. Ong *et al*. [15] used the URANS *k-ε* model for *Re*=1.0×10^6, 2.0×10^6 and 3.6×10^6 for the super critical and upper-transition flow regimes, and compare its results with those of Catalano et al. [13] and Singh and Mittal [14] which were in good agreement.

Yuce and Kareem [16] carried out studies of 2D circular and square cylinders for a wide range of Reynolds numbers from *Re*=2 to *Re*=4×10^6 using the *k-ω-SST* model, and found that the downstream wake of the square cylinder is substantially more turbulent than the circular one.

Among a few numerical results for *Re*> 10^7 reported in the published literature, those carried out on 3D flows are only a small part. Younis *et al*. [17] used the *k-ε* Standard and Re-Normalization Group (RNG) models on a mini Tension-Leg-Platform (TLP) on steady high Reynolds numbers from *Re*=8.8×10^6 to *Re*=6.0×10^7, to analyze the effects on the downstream pontoon and column. They found that the drag coefficient on the downstream column was only one tenth of its value for the upstream column because of the shielding effect. Vaz *et al*. [18] studied semi-empirical models to predict drag coefficients of an idealized SSP conformed by two square rounded-corner columns connected with a pontoon using the *k-ω-SST* viscosity model for *Re*=2.26×10^5, and identified that laminar-turbulent transition explain some of the deviations of the numerical results from experimental results.

Younis and Abrishamchi [19] investigated the turbulent flow around a 3D sectioned square cylinder at high Reynolds number (*Re*=1.0×10^4-1.0×10^5) using LES and URANS *k-ε* viscous model simulations, and concluded that URANS results are reliable as LES results but with lower cost in terms of computational resources. Dai *et al*. [20] use the *k-ε* model on a TLP at high Reynolds numbers from *Re*=1.79×10^5 to *Re*=7.5×10^6, and showed the accurate capabilities of open source software OpenFOAM to predict effects of turbulence as vortex shedding.

Rosetti *et al*. [21] studied the fluid-structure interaction of a rigid circular cylinder in 3D for *Re*<1.9×10^4 using the URANS *k-ω-SST* model that traditionally is studied in 2D, they showed that inertial effects play very important role in determining loads and motions. An *et al*. [22] tackled the LES model for 3D circular cylinders at high Reynolds numbers (*Re*=1.0×10^4-6.0×10^5), from the subcritical to the supercritical flow regime, where was found that shear layer instabilities play a major role in the transition to turbulence.

Recently, Bangga *et al*. [23] apply the RANS k-ω-SST model to a 3D flow through a circular cylinder mounted to a flat plate at Reynolds numbers from *Re*=1×10^6 to *Re*=8.4×10^6, and highlighted the importance of 3D simulations, due its strongly influence to the flow behavior near the joint. Ong *et al*. [24] studied the numerical flow around a monopile using the Spalart-All Delayed Detached Eddy Simulations (SADDES) at *Re*=4×10^6, and found that this numerical analysis can be useful to estimate the size and the location of the horseshoe vortex formation.

Based on the literature review about the flow interaction with square transversal section column with rounded and chamfer corners, their main efforts were focused on calculate drag force coefficients. However, from works analyzed on the literature review drag force coefficients for square transversal columns covers until *Re*=1.62×10^6, these on Tong et al. [10], as it was mentioned previously for this structures the characteristic Reynolds numbers are higher, then the relevance of this study is the 3D flow interaction and drag coefficients calculation for a SSP column.

The real scaled results can be useful for the election of corner radius for the configuration of semisubmersible platform legs.

ISSN 2448-5837

Numerical method details

The mass and momentum conservation equations for an incompressible fluid the RANS approach are as follows:

$$\frac{\partial u_i}{\partial x_i}=0 \qquad \text{Eq. 1}$$

$$\rho\left(\frac{\partial u_i}{\partial t}+\frac{\partial u_i u_j}{\partial x_i}\right)=-\frac{\partial p}{\partial x_i}+\frac{\partial}{\partial x_i}\left(\mu\left(\frac{\partial \mu_i}{\partial x_j}+\frac{\partial u_j}{\partial x_i}-\frac{2}{3}\delta_{ij}\frac{\partial u_l}{\partial x_l}\right)\right)+\frac{\partial}{\partial x_i}\left(-\rho\overline{u'_l u'_J}\right) \qquad \text{Eq. 2}$$

where u_i and u_j are the mean velocities, u'_i and u'_j are the fluctuating part of the velocity, p is the dynamic pressure, μ is the dynamic viscosity, δ_{ij} is the Kronecker delta, ρ is the density of fluid and $-\overline{\rho u'_i u'_j}$ is the Reynolds stress tensor which represents turbulence effects and introduces unknown by the averaging procedure. Then, by the Boussinesq hypothesis the Reynolds stress are modeled associating mean velocity gradients and introducing a turbulent viscosity, μ_t, and turbulent kinetic energy, t, as follows:

$$-\rho\overline{u'_l u'_J}=\mu_t\left(\frac{\partial u_i}{\partial x_j}+\frac{\partial u_j}{\partial x_i}\right)-\frac{2}{3}\left(\rho k+\mu_t\frac{\partial u_k}{\partial x_k}\right)\delta_{ij} \qquad \text{Eq. 3}$$

Finally, the turbulent viscosity (μ_t) can be obtained by solving additional transport equations (for example the *k-ε* or *k-ω* models), in this work we use the *k-ω-SST* model to achieve this.

The *k-ω-SST* turbulence model

The *k-ω-SST* turbulence model by Menter [25] [26] combines the *k-ω* model by Wilcox [27] in the near wall region and the standard *k-ε* model by Jones and Launder [28] in the outer region and the free shear layers.

The *k* and *ω* transport equations in the *k-ω-SST* model by Menter [25] [26] are as follows:

$$\frac{\partial(\rho k)}{\partial t}+\frac{\partial(\rho k u_i)}{\partial x_i}=\frac{\partial}{\partial x_i}\left[(\mu+\mu_t\sigma_k)\frac{\partial k}{\partial x_i}\right]+\tilde{G}_k+Y_k \qquad \text{Eq. 4}$$

$$\frac{\partial(\rho\omega)}{\partial t}+\frac{\partial(\rho\omega u_1)}{\partial x_1}=\frac{\partial}{\partial x_j}\left[(\mu+\mu_t\sigma_\omega)\frac{\partial \omega}{\partial x_j}\right]+\tilde{G}_\omega+Y_\omega+D_\omega \qquad \text{Eq. 5}$$

where $(\mu+\mu_t\sigma_k)$ and $(\mu+\mu_t\sigma_\omega)$ represent the k and ω effective diffusivities, respectively. Also, σ_k and σ_ω represent the Prandtl numbers for k and ω, respectively, $\tilde{G}_k$ represents the generation of turbulence by kinetic energy due to mean velocity gradients, $\tilde{G}_\omega$ represents the generation of ω, Y_k and Y_ω represent the diffusivity by turbulence of k and ω and D_ω represents the cross-diffusion term.

Now, from Menter [25] [26] let ϕ_1 represent any constant in the original model (σ_{k1},…) and ϕ_2 any constant in the transformed *k-ε* model (σ_{k2},…), then the relation between these terms is:

$$\phi=F_1\phi_1+(1-F_1)\phi_2 \qquad \text{Eq. 6}$$

where the function F_1 is defined as follows:

$$F_1=tanh\left(arg_1^4\right) \qquad \text{Eq. 7}$$

with,

$$arg_1=min\left(max\left(\frac{\sqrt{k}}{0.09\omega y},\frac{500\mu}{\rho y^2\omega}\right),\frac{4\rho\sigma_{\omega 2}K}{D_\omega y^2}\right) \qquad \text{Eq. 8}$$

and the cross-diffusion term D_ω is:

$$D_\omega=max\left(\rho\sigma_{\omega 2}\frac{1}{\omega}\frac{\partial k}{\partial x_j}\frac{\partial \omega}{\partial x_j},10^{-20}\right) \qquad \text{Eq. 9}$$

This term actually represents the difference between the original *k-ω* and the *k-ω-SST* model.

The *k-ω-SST* turbulence model is used to solve the viscous flow interaction by ANSYS-FLUENT 17.2 into a steady state simulation using a pseudo transient approach to calculate drag coefficient (*Cd*) on a 3D square column and analyze its flux behavior by the column presence.

Finally, the drag coefficient (*Cd*) is defined as follows:

$$Cd=\frac{F_y}{\frac{1}{2}\rho v^2 A_y} \qquad \text{Eq. 10}$$

where F_y is the drag force, ρ is the density, v is the velocity from the inlet flow and A_y is the projected area normal to the inlet velocity.

Numerical study

The approach of this numerical study is to consider the column geometry of a SSP, to optimize the ratio *R/D* in order to minimize the drag force on the column with square transversal section for very high Reynolds numbers (Re=4.09×10^6-4.91×10^7). The column characteristic dimension is D=17.2*m* and the draft is 27.5*m* (submerged part of the column) which has similar dimensions of the Na Kika SSP [29] for British Petroleum in the Gulf of Mexico and the flow velocities considered are U = 0.25, 0.5, 0.75, 1.0, 1.5, 2.0, 2.5 and 3 *m/s*.

To achieve numerical simulations is remarkable the use of a steady state approach to reduce the high computational time

Edición digital

ISSN 2448-5837

spent on transient simulations. To validate the results, one mesh convergence test and two scaled tests for low Reynolds numbers were developed, showing that the presented results are in close agreement with published values by others.

Finally, in order to provide an archive of drag coefficients for columns of various curvature ratios on post critical Reynolds number the present study fills the Reynolds number gap between Re=4.09×10^6-4.91×10^7, with curvature radius R=1.0, 1.25, 1.5, 2.0, 3.0 and 4.0 *m*. Therefore, it must be emphasized that main focus of this study is the calculation of drag coefficients and does not report any lift coefficient data.

Geometrical domain and boundary conditions

The geometric domain is showing in Fig. 1, and three domain divisions are defined; in the domain-*A* is located a coarse mesh, in domain-*B* is a medium size mesh and in the domain-*C*, on the column and its boundary is a fine mesh. The mesh size is defined by the maximum grid size on the domain and the growth between the domains is geometrical, $B_{size}=2{*}C_{size}$ and $A_{size}=2{*}B_{size}$.

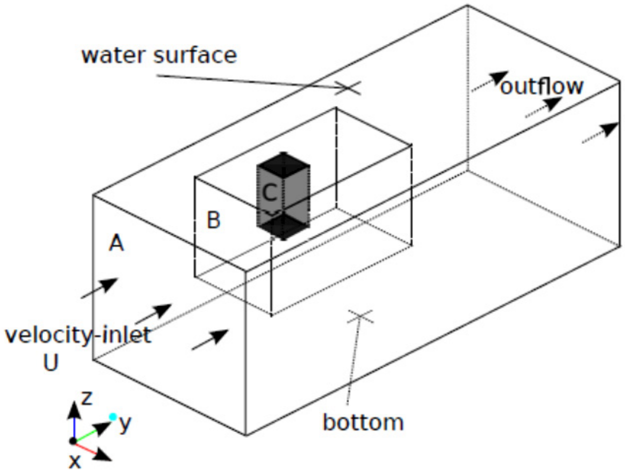

Figure 1. Geometry, computational domain, boundary conditions and domain divisions A, for a coarse mesh, B, for a medium size mesh and C, for a fine mesh.

The main domain dimensions and boundary conditions where the flow passes from left to right over the domain is shown in Fig. 2. In this work, the distance from the column to domain boundaries was determined after some tests in which was observed a uniform field distribution close to the flow inlet and a fully developed flow at the outlet. The distance to side and bottom boundaries were determined considering these boundaries have no effects on the flow around the column. The distance to the domain boundaries change from author to author and depends on the column dimensions, grid size and flow velocities.

ISSN 2448-5837

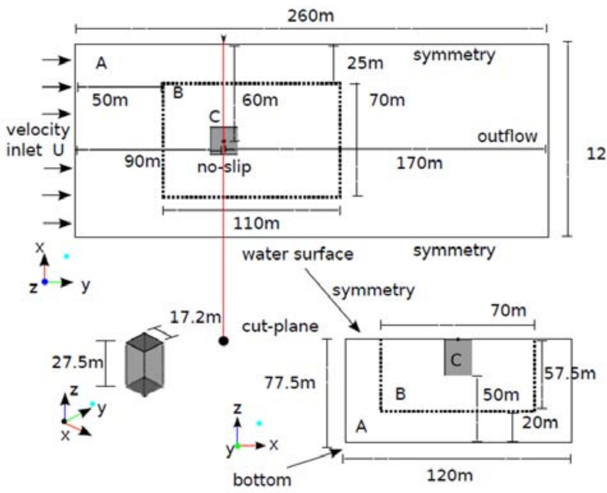

Figure 2. Domain dimensions and boundary conditions

The flow inlet is located around 5∗*D* upstream from the center of the column, and the flow outlet is located around 10∗*D* downstream from the center of the column; it must be noted that these distances are sufficient to eliminate the far field effects on the flow. The distance to side boundaries is located around 3∗*D* from the center of the column. Finally, the distance to the bottom of the domain is located around 3∗*D* from the bottom of the column; this value is sufficient to cover the flow vertical effects by the column presence, because the changes in the main flow are in the horizontal plane. The boundary conditions used for the numerical simulations are as follows:

(1) Uniform flow is specified at the inlet, $\vec{U}=(u,v,w)=(0,v,0)$.

(2) Symmetry condition is applied on both sides, upper and bottom boundaries (zero normal velocity at the symmetry plane, for example, if normal is at (1,0,0), velocity vector restriction is $(u,v,w)=(0,v,w)$, the same for zero normal gradients).

(3) No-slip condition is applied on the column surface, $\vec{U_c}=(u,v,w)=(0,0,0)$

(4) Along the outflow boundary is fully-developed turbulent flow with zero diffusion flux condition at the boundary, $J=-cD_n\nabla Ø$, where J is the diffusion flux, c is total concentration, and D_n is the diffusion coefficient on the n normal direction and Ø is the flow variable (Pressure, temperature, turbulence, ...).

Convergence mesh tests

The number, size and quality of the mesh elements dictate the accuracy of the solutions. Then, it is critical to ensure that the solutions are not adversely affected by such factors. To achieve this goal, a three-level mesh refinement study was completed. In this study, the number of elements was systematically increased until the drag coefficients (Cd) results were no longer dependent upon the mesh size, see geometric domain (Fig. 1).

In this study, three mesh resolutions are employed to test its effects on the results, these resolutions are denoted as: MI ($0.3m\times0.6m\times2.4m$), MII ($0.4m\times0.8m\times3.2m$) and MIII ($0.5m\times1.0m\times4.0m$). The mesh resolution notation express the maximum grid size per zone, i.e., on MI the maximum grid size in zone C is $C_{size}=0.3m$, in zone B is $Bsize=0.6m$ and in zone A is $A_{size}=2.4m$. Mesh resolutions MI, MII and MIII contain around 2191679, 1187711 and 926781 elements, respectively. The samples of the MI, MII and MIII meshes are shown in Fig. 3.

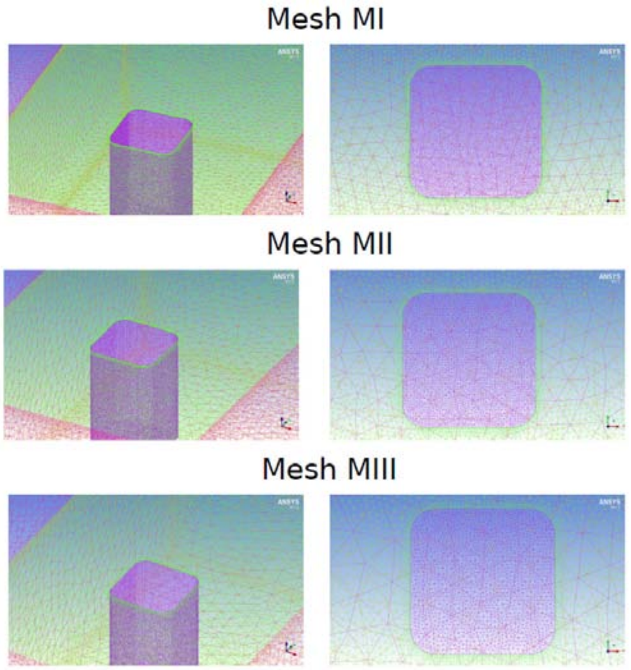

Figure 3. Mesh samples for convergence test:
Mesh *MI* (0.3*m*,0.6*m*,2.4*m*), Mesh *MII* (0.4*m*,0.8*m*,3.2*m*) and
Mesh *MIII* (0.5*m*,1.0*m*.4.0*m*).

All simulations consider seawater at 20°*C*, with density and dynamic viscosity of 1024.81 kg/m^3 and 1.077×10^{-3} $Pa.s$ respectively (from the International Towing Tank Conference, ITTC 2011 [30]).

In order to span a large and relevant range of Reynolds numbers, multiple inlet sea water velocity values were used. The selected values were U=0.25, 0.5, 0.75, 1.0, 1.5, 2.0, 2.5 and 3.0 m/s. This covers a range for Reynolds number between approximately $Re=4.09\times10^6$-4.91×10^7.

A grid convergence study has been carried out with three sets of meshes previously described (MI, MII and MIII) for curvature ratios R/D=1/17.2, 2/17.2, 3/17.2 and 4/17.2. In that conditions we can compare the drag coefficients (Cd) for the convergence test, and the relative change between MII-MI($\Delta_{II\text{-}I}=|100*(Cd_{MII}-Cd_{MI})|/Cd_{MI}$) and MIII-MI($\Delta_{III\text{-}I}=|100*(Cd_{MIII}-Cd_{MI})|/Cd_{MI}$).

The main results related with the convergence mesh tests including the drag coefficient and the relative change between the different models meshes are shown from Table 1 thru 4. In 1, for R/D=1/17.2 the relative change between MII-MI and MIII-MI remains under 8.2%. For R/D=2/17.2, in Table 2, the maximum relative change in MII-MI is 4.6% and for MIII-MI is 9.6%. For R/D=3/17.2, in Table 3, the relative change in MII-MI remains under 4.7%, and only for $Re=2.45\times10^7$ the relative change is around 10% and for MIII-MI the relative change remains under 5.3%, and only for $Re=2.45\times10^7$ and $Re=3.27\times10^7$ the relative change have significant differences around to 16%.

Finally, for R/D=4/17.2, in Table 4, the relative change in MII-MI remains under 3.9%, and only for $Re=3.27\times10^7$ the relative change is around 10% and in the case of MIII-MI for $Re<2.45\times10^7$ the relative change remains under 7.0%, however for $Re\geq2.45\times10^7$ the relative change have significant differences from 14.6% to 20.2%.

Table 1: Drag coefficients in grid convergence test, $R=1m$ ($R/D=0.058$).

Re	MI	MII	MIII	$\Delta._{II-I}$ (%)	Δ_{III-I} (%)
4.09×10^6	0.949	1.020	0.971	7.4	2.3
8.18×10^6	0.927	0.942	0.945	1.6	1.9
1.22×10^7	0.958	0.986	0.975	2.9	1.7
1.63×10^7	0.976	0.997	0.994	2.1	1.8
2.45×10^7	0.995	1.063	1.008	6.8	1.3
3.27×10^7	1.015	1.035	0.999	1.9	1.5
4.09×10^7	1.016	1.085	1.100	6.7	8.2
4.91×10^7	1.049	1.070	1.125	2.0	7.2

Table 2: Drag coefficients in grid convergence test, R = 2m (R/D = 0.116).

Re	MI	MII	MIII	Rel.Ch.$_{II-I}$ (%)	Rel.Ch. III–I (%)
4.09×10^6	0.451	0.460	0.468	1.9	3.7
8.18×10^6	0.413	0.432	0.453	4.6	9.6
1.22×10^7	0.407	0.417	0.432	2.4	6.1
1.63×10^7	0.402	0.414	0.425	2.9	5.7
2.45×10^7	0.413	0.417	0.442	0.9	7.0
3.27×10^7	0.415	0.425	0.435	2.4	4.8
4.09×10^7	0.402	0.404	0.420	0.4	4.4
4.91×10^7	0.405	0.424	0.428	4.6	5.6

Table 3: Drag coefficients in grid convergence test, R = 3m (R/D = 0.174).

Re	MI	MII	MIII	Rel.Ch. $_{II-I}$ (%)	Rel.Ch. $_{III-I}$ (%)
4.09×10^6	0.438	0.417	0.441	4.7	0.6
8.18×10^6	0.382	0.390	0.402	2.0	5.2
1.22×10^7	0.379	0.372	0.391	1.8	3.1
1.63×10^7	0.373	0.383	0.393	2.6	5.3
2.45×10^7	0.374	0.411	0.436	9.8	16.5
3.27×10^7	0.372	0.370	0.432	0.5	16.1
4.09×10^7	0.370	0.376	0.370	1.6	0.0
4.91×10^7	0.363	0.364	0.363	0.2	0.0

Table 4: Drag coefficients in grid convergence test, R = 4m (R/D = 0.232).

Re	MI	MII	MIII	Rel.Ch.$_{II-I}$ (%)	Rel.Ch.$_{III-I}$(%)
4.09×10^6	0.405	0.409	0.396	0.9	2.2
8.18×10^6	0.376	0.368	0.379	2.1	0.7
1.22×10^7	0.362	0.350	0.371	3.3	2.4
1.63×10^7	0.356	0.352	0.381	1.1	7.0
2.45×10^7	0.344	0.354	0.405	2.9	17.7
3.27×10^7	0.354	0.391	0.413	10.4	16.6
4.09×10^7	0.363	0.370	0.416	1.9	14.6
4.91×10^7	0.356	0.342	0.428	3.9	20.2

From these convergence mesh tests, we observe that mesh resolution MIII for curvature radius R < 3m has drag coefficient values close to MI (Δ_{III-I}<10%) and mesh resolution MII has values close to MI (Δ_{II-I}≤10%) for all the curvature radius tested, the MII mesh resolution shows closer drag coefficient values. Then, the MI mesh resolution results were no longer dependent upon the mesh, because the low differences between MI and MII refinements, then the MI mesh resolution was selected to be used on the following analysis.

Scaled tests for low Reynolds numbers

The model and domain were scaled to estimate drag coefficient values for low Reynolds number (1.63×10^4-4.91×10^6). The scaled models were used in order to the flow velocities has a physical meaning, because if we use the real scale model for those low Reynolds numbers the flow velocities used will be too low to have a physical meaning. We used those scaled tests to reproduce drag coefficient values and drag crisis region included in the literature to compare our results.

ISSN 2448-5837

Two scaled tests for the curvature ratio R/D=3/17.2=0.174, R/D=0.3/1.72 and R/D=0.03/0.172 were driven, where scaled mesh resolutions employed are 0.03m×0.06m×0.24m and 0.003m×0.006m×0.024m respectively.

In these tests the flow velocities were from 0.1m/s to 3.0m/s and those velocities cover Reynolds numbers from Re=1.63×10^4 to Re=4.91×10^7, results are shown in Fig. 4 and a continuous behavior is observed even with the scaled curvature ratios R/D=3/17.2, R/D=0.3/1.72 and R/D=0.03/0.172.

Moreover, the calculated drag coefficient values are compared with experimental data by Delany and Sorensen [31] for curvature ratios R/D=0.167 and R/D=0.333, where the experiment with the first curvature ratio was driven for one square transversal section D=0.3048m and the second with two square transversal sections D=0.3048m and D=0.1016m. These results show that the calculated drag coefficient values are of the same order than the experimental values, the drag crisis curve of the calculated drag values for R/D=0.174 is around Re=1×10^5 and the experimental drag values for R/D=0.167 is around Re=5×10^5, the latter difference could related with the different ratios R/D.

Results

Drag coefficients

In this section the curvature radius R=1.25m and R=1.5m were used to review the drag coefficient behavior in the transition gap between curvature radius R=1m and R=2m, these only for mesh resolution MI. In Fig. 5, a comparison of the drag coefficients for the curvature radius in function of the Reynolds number is shown. In this figure, it shows the fast transition of the drag coefficients obtained for R=1m (cyan

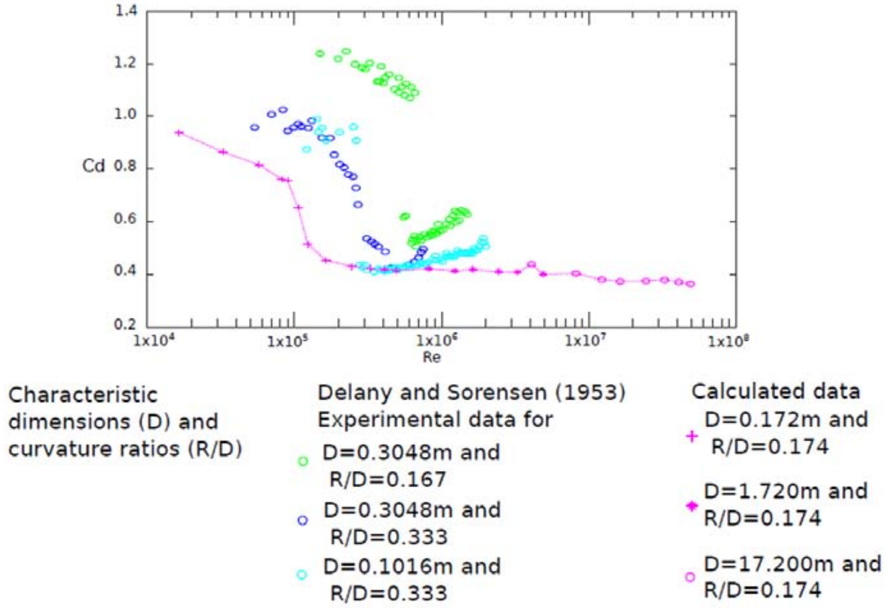

Figure 4. Drag coefficient values calculated for curvature ratios R/D=3/17.2 =0.174 and scaled tests, R/D=0.3/1.72 and R/D = 0.03/0.172 and compared with Delany and Sorensen (1953) experimental data with curvature ratios R/D=0.167 and R/D= 0.333

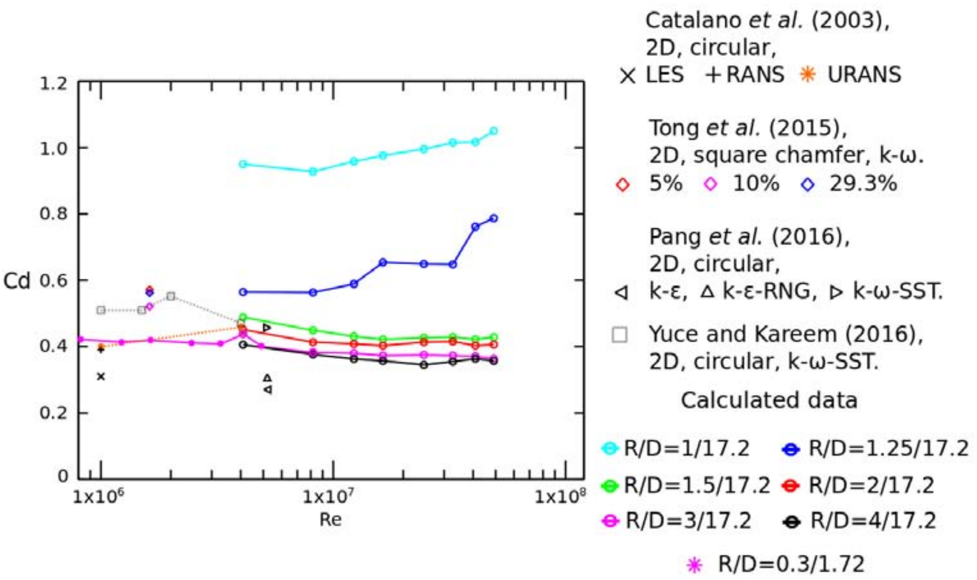

Figure 5. Comparison of calculated drag coefficient (Cd) as a function of Reynolds number with numerical data by Catalano et al. (2003), Tong et al. (2015), Pang et al. (2016) and Yuce and Kareem (2016).

line), to *R*=1.25*m* (blue line), which has a reduction between 24% to 40% and the transition from *R*=1.25*m* (blue line) to *R*=1.5*m* (green line), which has a reduction between 13% to 45%. Also, we can observe that drag coefficients for *R*=1*m* and *R*=1.25*m* have an increasing behavior as Reynolds number increases, while the other curvature radius has a decreasing behavior.

Moreover, from Fig. 5, we can observe that the drag coefficients for *R*>1.25*m* have a reduction of around 10% from *R*=1.5*m* to *R*=2*m*, from *R*=2*m* to *R*=3*m* and from *R*=3*m* to *R*=4*m*, respectively.

Then, the principal decrease on drag coefficients values are from rounded corners ratio of *R/D*<2/17.2=0.116 that exhibit a decrease about 55% from *R*=1*m* (cyan line), to *R*=2*m* (red line). These analysis agree with the predicted decrease of drag coefficient values on square columns with rounded corners ratio of *R/D*≤0.15 by Okamoto and Uemura [2] and are in close agreement with the predicted decrease of drag coefficient values of the 60% by Tamura *et al*. [4].

Also, a comparison of our results with the drag coefficients obtained from the literature was made. We can observe that our results for the radius R=4m are in close agreement with drag coefficients calculated for 2D circular column simulations by Catalano et al. [13] for *Re*=1×10^6. Furthermore, our results of drag coefficients for *R*=2*m* to *R*=4*m* are around the drag coefficients calculated from *Re*=1×10^6 to *Re*=3.6×10^6 by Catalano et al. [13] and Yuce and Kareem [16] for 2D circular column simulations.

From the same Fig. 5, we can observe from our results, the decreasing values of drag coefficients related with the increment of curvature radius are similar to the results obtained by Pang et al. [32] for a 2D circular cylinder at higher Reynolds numbers (*Re*=5.2×10^6). Additionally, to compare the effect of curvature radius in drag coefficient reduction versus chamfer on the columns square section, it is shown the drag coefficients by Tong et al. [10] of flow past 2D chamfer square column *Re*=1.6×10^6 and it is observed that is more efficient the curvature radius with ratio *R/D*=0.3/1.72 than chamfer, at this Reynolds number.

Finally, the drag coefficients values in function of the curvature ratio *R/D* are shown in Fig. 6. It is observed a monotonic decrease in the drag coefficients when the curvature ratio increases independently of the Reynolds number, this decrement in the drag coefficient is more significant between *R/D*=0.5 and 0.10. This behavior is similar at the results presented by Tanaka et al. [33] for rectangular columns. Also, we can compare the drag coefficient as a function of the chamfer radius increment by Tong et al. [10] for *Re*=1.62×10^6 which considers the chamfer value of 29.3% as an octagonal column, from this we can confirm that the reduction of drag coefficients is more effective by the curvature radius introduction.

Flow patterns

It is illustrative to show a select set of flow patterns for different curvature ratios *R/D*=1/17.2, 2/17.2 and 4/17.2, for various flow velocity scenarios *Re*=4.09×10^6, 1.63×10^7 and 4.91×10^7, Fig. 7 to 15, these figures are only for the mesh resolutions MI and for the B and C zones from the domain (Fig. 1 and 2). As the flow patterns changes in function of the different horizontal planes we select several reference planes to capture the flow behavior: one vertical plane at the middle of the column and normal to the *x-axis* (*Xfxp*), one vertical plane at 10*m* from the backward end of the column and normal to the *y-axis* (*Yfxp*) and two horizontal planes at 10*m* and 20*m* above the lower end of the column and normal to the z-axis ($Zfxp_1$ and *Zfxp2*, respectively).

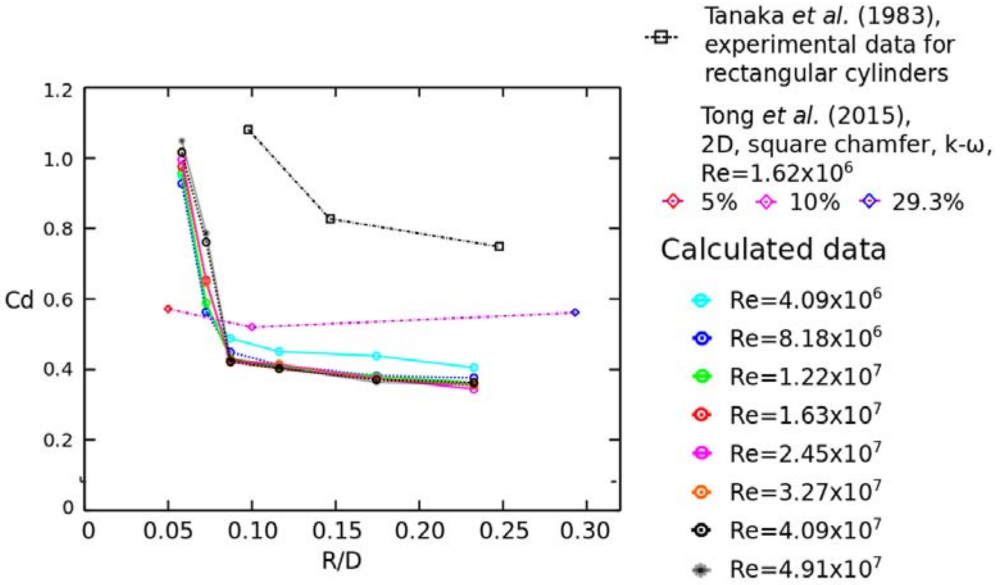

Figure 6. Comparison of calculated drag coefficient (Cd) as a function of corner radius ratio (R/D) with experimental results by Tanaka et al. (1983) and numerical data by Tong et al. (2015).

The results, provided in Fig. 7 to 15 at plane *Xfxp* show that the flow behavior developed in the lower boundary of the B zone domain is not affected by the column flux, i.e., velocity flow is unaltered by the column presence (this boundary has the same velocity as the inlet boundary). Also, at plane *Yfxp* we can observe a similar behavior at the side boundaries of the B zone domain.

Moreover, from the curvature ratio increases and flow pattern behavior, we can highlight:

For the curvature ratio *R/D*=1/17.2, Fig. 7 to 9 , at the plane *Yfxp* the trail after the column conserves its trace even if the Reynolds number increases, however in the *Xfxp* plane is shown that turbulence trace seems to increase as the Reynolds number increases, which causes the presence of several eddies on *Xfxp* and *Yfxp* planes. Also, the trace is distorted far from the column as it approaches to the surface, these is shown on the transition between $Zfxp_1$ and $Zfxp_2$ planes.

ISSN 2448-5837

Edición digital

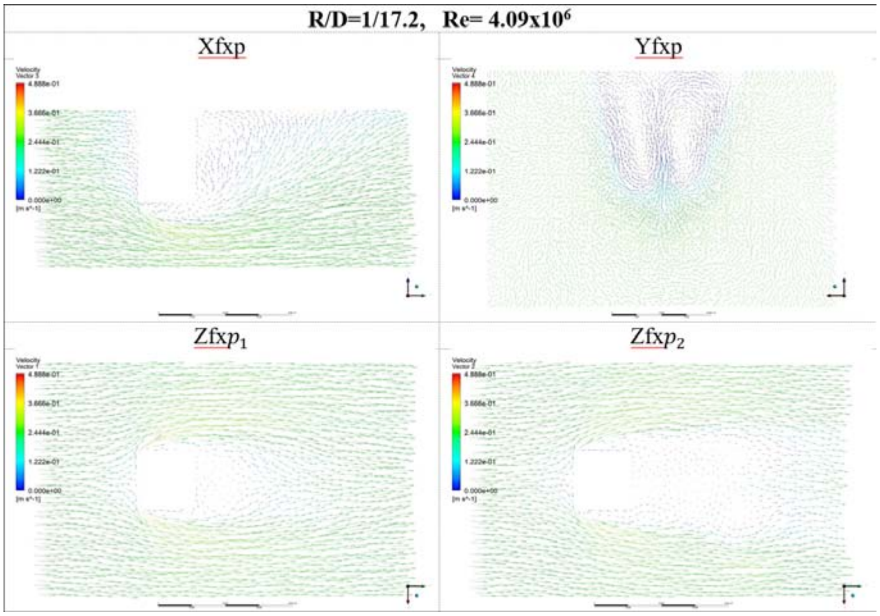

Figure 7. Velocity flow fields for fixed planes into B and C zones of the domain (Fig. 1 and 2), *Xfxp* at the middle of the column, Yfxp at 10m from the end of the column, $Zfxp_1$ and $Zfxp_2$ at 10*m* and 20*m* of elevation from the bottom of the column.

ISSN 2448-5837

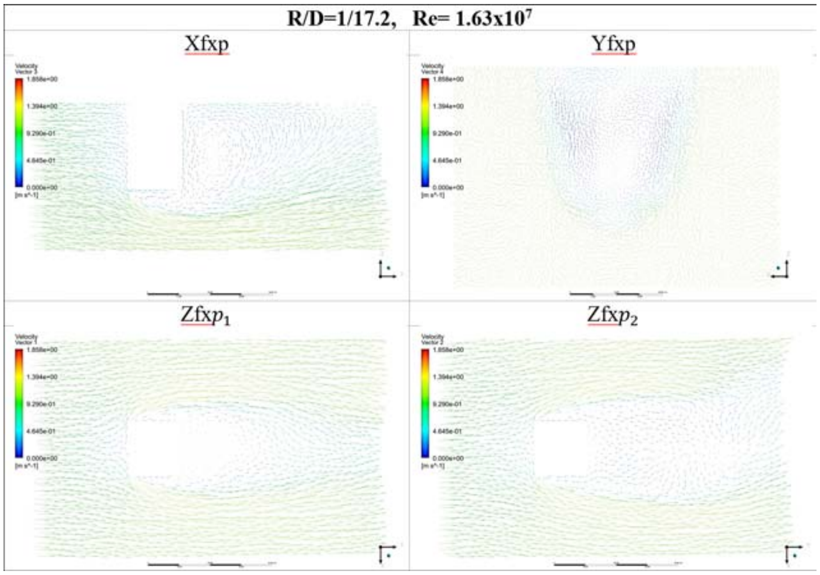

Figure 8. Velocity flow fields for fixed planes into B and C zones of the domain (Fig. 1 and 2), *Xfxp* at the middle of the column, *Yfxp* at 10*m* from the end of the column, *Zfxp*$_1$ and *Zfxp*$_2$ at 10*m* and 20*m* of elevation from the bottom of the column.

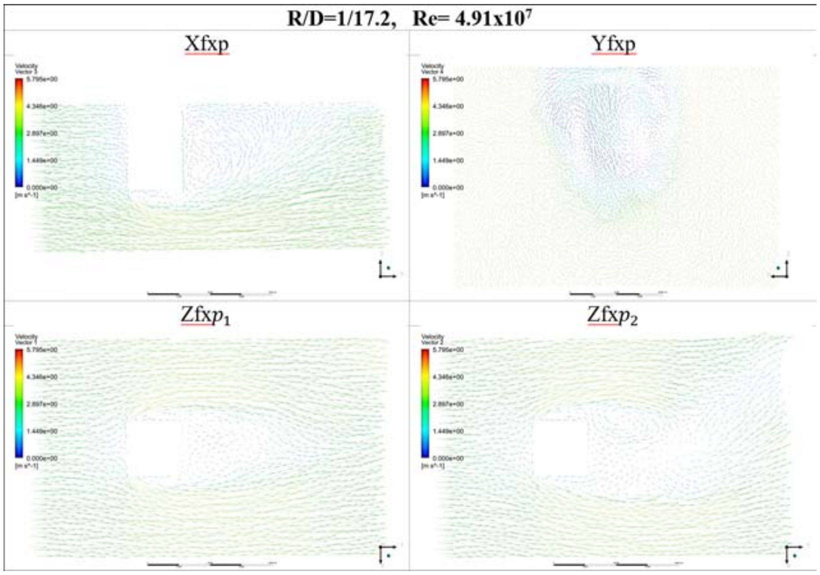

Figure 9. Velocity flow fields for fixed planes into B and C zones of the domain (Fig. 1 and 2), *Xfxp* at the middle of the column, *Yfxp* at 10m from the end of the column, *Zfxp*$_1$ and *Zfxp2* at 10*m* and 20*m* of elevation from the bottom of the column.

For the curvature ratio *R/D*=2/17.2, Fig. 10 to 12, the trail after the column reduces its trace as the Reynolds number increases, this is more evident in the $Zfxp_1$ plane. The flux cannot regain as it approaches to the surface (see the $Zfxp_2$ plane), for that reason the trace trail enlarge at this zone (see the *Yfxp* plane).

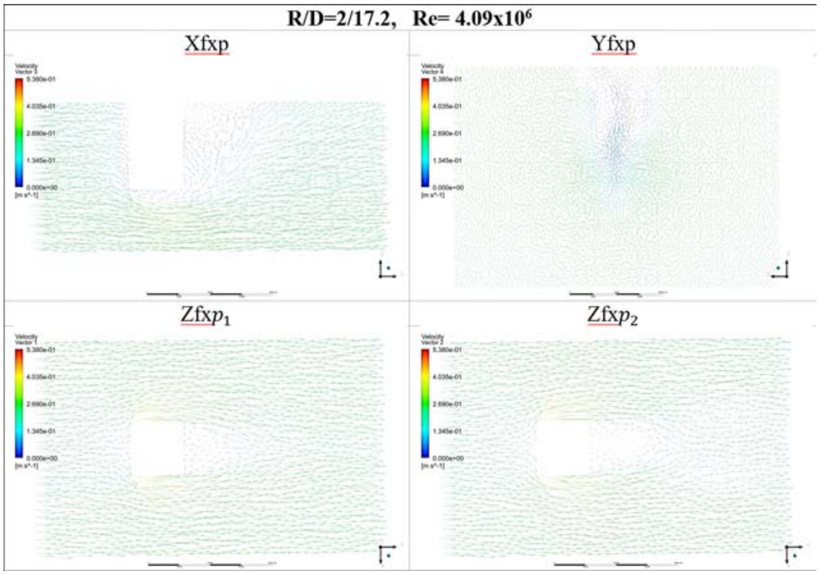

Figure 10. Velocity flow fields for fixed planes into B and C zones of the domain (Fig. 1 and 2), *Xfxp* at the middle of the column, *Yfxp* at 10*m* from the end of the column, $Zfxp_1$ and $Zfxp_2$ at 10*m* and 20*m* of elevation from the bottom of the column.

ISSN 2448-5837

Edición digital

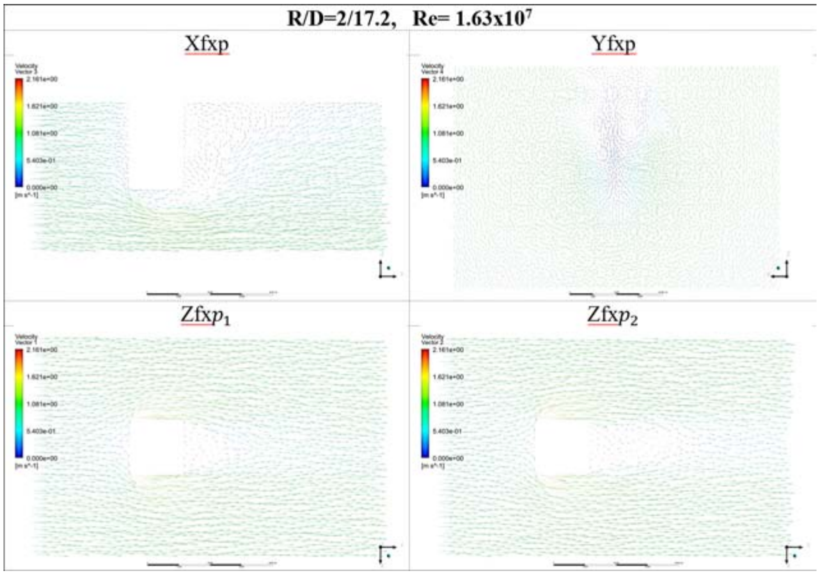

Figure 11. Velocity flow fields for fixed planes into B and C zones of the domain (Fig. 1 and 2), *Xfxp* at the middle of the column, *Yfxp* at 10*m* from the end of the column, $Zfxp_1$ and $Zfxp_2$ at 10*m* and 20*m* of elevation from the bottom of the column.

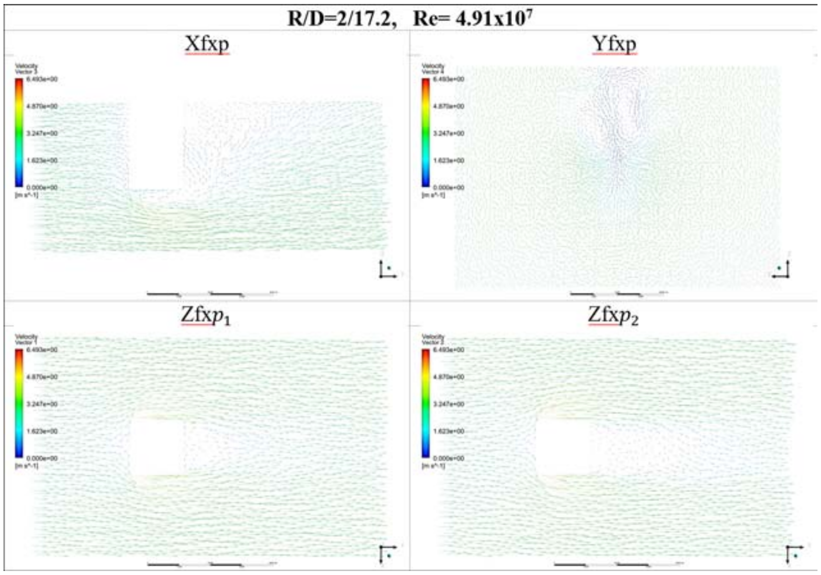

Figure 12. Velocity flow fields for fixed planes into B and C zones of the domain (Fig. 1 and 2), *Xfxp* at the middle of the column, *Yfxp* at 10*m* from the end of the column, $Zfxp_1$ and $Zfxp_2$ at 10*m* and 20*m* of elevation from the bottom of the column.

In Fig. 13 to 15, for the curvature ratio *R/D*=4/17.2 the trail after the column conserves its thin trace even if the Reynolds number increases, probably caused by its streamlined shape and the evident reduction of eddy formation. These eddy presence decrease is also shown for *R/D*=1/17.2 and *R/D*=2/17.2.

ISSN 2448-5837

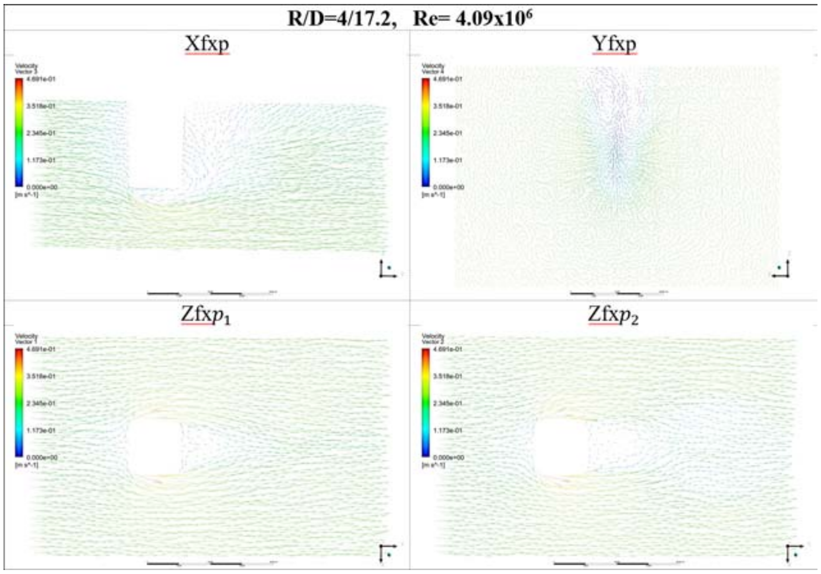

Figure 13. Velocity flow fields for fixed planes into B and C zones of the domain (Fig. 1 and 2), *Xfxp* at the middle of the column, *Yfxp* at 10*m* from the end of the column, $Zfxp_1$ and $Zfxp_2$ at 10*m* and 20*m* of elevation from the bottom of the column.

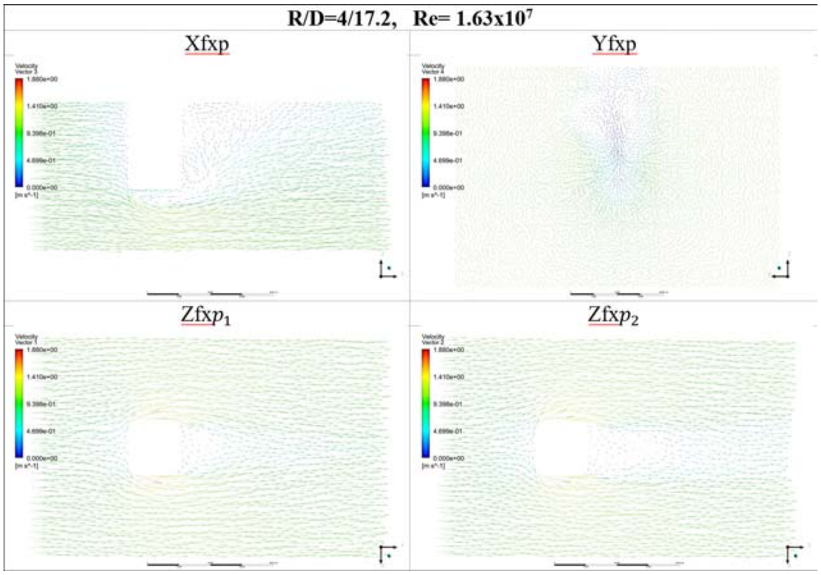

Figure 14. Velocity flow fields for fixed planes into B and C zones of the domain (Fig. 1 and 2), *Xfxp* at the middle of the column, *Yfxp* at 10*m* from the end of the column, $Zfxp_1$ and $Zfxp_2$ at 10*m* and 20*m* of elevation from the bottom of the column.

ISSN 2448-5837

Edición digital

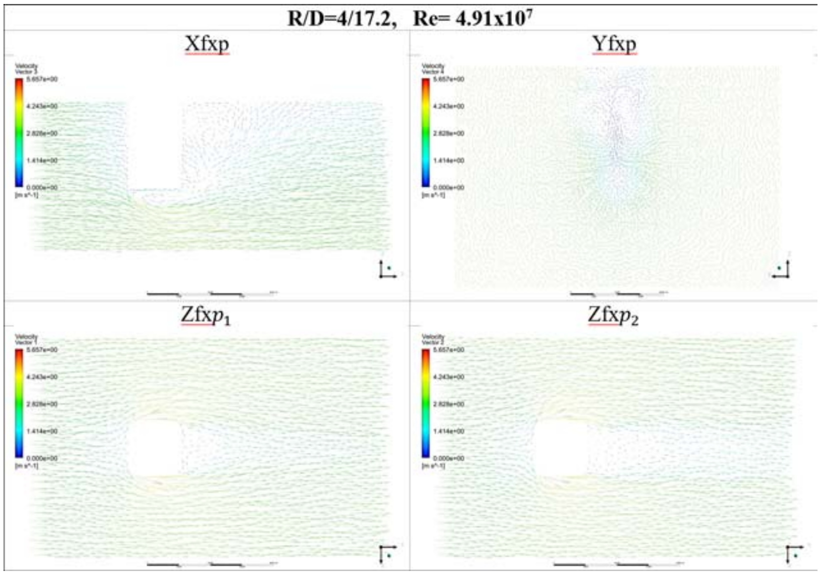

Figure 15. Velocity flow fields for fixed planes into B and C zones of the domain (Fig. 1 and 2), *Xfxp* at the middle of the column, *Yfxp* at 10*m* from the end of the column, $Zfxp_1$ and $Zfxp_2$ at 10*m* and 20*m* of elevation from the bottom of the column.

Finally, to analyze the streamline behavior in function of the maximum velocity bound is shown in Table 5, the maximum velocity bound is associated with the velocity on the rounded corner in the column. These, because the analysis of Fig. 7 to 15 indicates this association. In Table 5, it is remarkable that the maximum velocity on rounded corner is reduced as the curvature ratio increases from R/D>2/17.2. These observations are in agreement with the drag coefficients results, Fig. 5, in which the variation of drag coefficient for curvature ratio R/D=1/17.2 shows bigger changes and reduces as the curvature ratio increases to R/D=2/17.2, and finally seems to stabilize at R/D>2/17.2.

Table 5: Maximum flow velocity in the region close to the corner of the column for curvature ratios: $R_1/D=1/17{:}2$, $R_2/D=2/17{:}2$, $R_3/D = 3/17{:}2$ and $R_4/D = 4/17{:}2$.

Re	Maximum flow velocity (m/s)			
	R_1/D	R_2/D	R_3/D	R_4/D
4.09×10^6	0.93	0.55	0.50	0.47
8.18×10^6	1.04	1.11	1.01	0.94
1.22×10^7	1.48	1.67	1.53	1.43
1.63×10^7	2.01	2.22	2.04	1.90
2.45×10^7	3.03	3.35	3.07	2.86
3.27×10^7	4.04	4.46	4.11	3.83
4.09×10^7	5.25	5.57	5.12	4.79
4.91×10^7	6.24	6.69	6.15	5.73

Conclusions

Drag coefficient values (Cd) were calculated from various different curvature ratios R/D=1/17.2, 1.25/17.2, 1.5/17.2, 2/17.2, 3/17.2 and 4/17.2 on a 3D column with square transversal section for very high Reynolds numbers (Re=4.09×10^6-4.91×10^7). This represents an archival dataset of drag coefficient results for the problem of 3D square column sections with rounded corners in cross flow, which are commonly used in SSP for the oil and gas industry. These findings are in good agreement compared with the values reported in the literature for lower Reynolds numbers.

The impact of drag coefficient values in function of Reynolds number, our results show that there is a significant decrease of the drag coefficient values for ratios intervals R/D=1/17.2 to 1.25/17.2 and R/D=1.25/17.2 to 1.5/17.2, which has a reduction between 24% to 40% and 13% to 45% (for Reynolds number range considered in this study), respectively. However, it is important to highlight that for ratios R/D>1.5/17.2 a slight decrease in drag coefficient values is shown as curvature radius increases. These agree with the results by Okamoto and Uemura [2] and Tamura et al. [4] for square transversal section columns with rounded corners.

Flow patterns analysis show that the trail trace and eddy formation reduces as the corner radius curvature increases, these would help to study the effect over columns pairs (shielding effect) as in SSP.

According to the results obtained in this work is remarkable that steady state simulations provides a valuable information that can be obtained with a significant less computational time in comparison with the transient simulations. However, steady state simulation cannot substitute transient simulation because the variable behavior under vortex shedding. This kind of studies can be a support to select the curvature radius for SSP columns in an early design phase, based on reduce the current drag forces on the hull.

Future work will include a further study on unsteady simulations for vortex shedding analysis and current drag forces on the hull due columns and pontoons interactions.

Acknowledgments

The authors wish to acknowledge the support provided by the Instituto Mexicano del Petróleo (IMP). This study was carried out with funds of Fondos Sectoriales CONACYT-SENER-Hidrocarburos thru the Deepwater Technology Research Center (Centro de Tecnología para Aguas Profundas, CTAP-IMP).

The author J. Sanchez-Mondragon thanks to Dirección de Cátedras CONACYT for the financial support granted during the research included in this manuscript.

Support for the author Oscar A. Godoy-Marroquin was provided by Fondos Sectoriales CONACYT-SENER-Hidrocarburos thru the Deepwater Technology Research Center (Centro de Tecnología para Aguas Profundas, CTAP-IMP).

References

[1] Bearman, P. W., Graham, J. M. R., Obasaju, E. D., Drossopoulos G. M., 1984, "*The influence of corner radius on the forces experienced by cylindrical bluff bodies in oscillatory flow*," Applied Ocean Research 6(2), pp. 83-89.

[2] Okamoto, S., Uemura, N., 1991, "*Effect of rounding side-corners on aerodynamic forces and turbulent wake of a cube placed on a ground plane*," Experiments in Fuids 11(1), pp. 58-64.

[3] Kawai, H., 1998, "*Effect of corner modifications on aeroelastic instabilities of tall buildings*," Journal of Wind Engineering and Industrial Aerodynamics 74-76, pp. 719-729.

[4] Tamura, T., Miyagi, T., Kitagishi, T., 1998, "*Numerical prediction of unsteady pressures on a square cylinder with various corner shapes*," Journal of Wind Engineering and Industrial Aerodynamics 74-76, pp. 531-542.

[5] Miran, S., Sohn, C. H., 2015, "*Numerical study of the rounded corners effect on flow past a square cylinder*," International Journal of Numerical Methods for Heat and Fluid Flow 25(4), pp. 686-702.

[6] Miran, S., Sohn, C. H., 2016, "*Numerical investigation of the effect of corner radius on forced oscillating square cylinder*," Journal of Applied Fluid Mechanics 9(6), pp. 3013-3022.

[7] Ong, M. C., 2012, "*Unsteady RANS simulation of flow around a 5:1 rectangular cylinder at high reynolds numbers*," Proceedings of the ASME 2012 31st, International Conference on Ocean, Offshore and Artic Engineering, Rio de Janeiro, Brazil, July 1-6. (OMAE2012-83719)

[8] Tian, X., Ong, M. C., Yang, J., Myrhaug, D., 2013, "*Unsteady RANS simulations of flow around a rectangular cylinders with different aspect ratios*," Ocean Engineering 58, pp. 208-216.

[9] Sohankar, A., 2014, "*A LES study of the flow interference between tandem square cylinder pairs*," Theoretical and Computational Fluid Dynamics 28, pp. 531-548.

[10] Tong, J. C. K., Abraham, J. P., Tse, J. M., Sparrow, E. M., 2015, "*Using corner chamfers to reduce the drag of flat-sided columns*," Proceedings of the Institution of Civil Engineers: Engineering and Computational Mechanics 168(2), pp. 79-88.

[11] Dai, S. S., Younis, B. A., Zhang, H. Y., Zhang, R. Y., 2016, "*Numerical simulation of the influence of rounded corners on flow around a square column*," Proceedings of the ASME 2016 35th, International Conference on Ocean, Offshore and Artic Engineering, Busan, South Korea, June 19-24. (OMAE2016-54512)

[12] Wang, M., Catalano, P., Iaccarino, G., 2001, "*Prediction of high Reynolds number flow over a circular cylinder using LES with wall modeling*," Center for Turbulence Research Annual Research Briefs, pp. 45-50.

[13] Catalano, P., Wang, M., Iaccarino, G., Moin, P., 2003, "*Numerical simulation of the flow around a circular cylinder at high Reynolds numbers*," International Journal of Heat and Fluid Flow 24, pp. 463-469.

[14] Singh, S. P., Mittal, S., 2005, "*Flow past a cylinder: Shear layer instability and drag crisis*," International Journal for Numerical Methods in Fluids 47(1), pp. 75-98.

[15] Ong, M. C., Utnes, T., Holmedal, L. E., Myrhaug, D., Pettersen, B., 2009, "*Numerical simulation of flow around a smooth circular cylinder at very high Reynolds numbers*," Marine Structures 22, pp. 142-153.

[16] Yuce, M. I., Kareem, D. A., 2016, "*A numerical analysis of fluid flow around circular and square cylinders*," American Water Works Association 108(10), pp. E546-E554.

[17] Younis, B. A., Teigen, P., Przulj, V. P., 2001, "*Estimating the hydrodynamic forces on a mini TLP with computational fluid dynamics and design-code techniques*," Ocean Engineering 28, pp. 585-602.

[18] Vaz, G., Waals, O. J., Ottens, H., Fathi, F., Souëf, T. L., Kiu, K., 2009, "*Current affairs: Model tests, semi-empirical predictions and CFD computations for current coefficients of semi-submersibles*," Proceedings of the ASME 2009 28th, International Conference on Ocean, Offshore and Artic Engineering, Honolulu, Hawaii, USA, May 31 - June 5. (OMAE2009-80216)

[19] Younis, B. A., Abrishamchi, A., 2014, "*Three-dimensional turbulent vortex shedding from a surface-mounted square cylinder: Predictions with Large-Eddy Simulations and URANS*," J. Fluid Eng. 136(6), Paper No. 060907.

[20] Dai, S., Younis, B. A., Sun, L., 2015, "*OpenFOAM predictions of hydrodynamics loads on full-scale TLP*," Ocean Engineering 102, pp. 162-173.

[21] Rosetti, G. F., Vaz, G., Condino-Fujarra, A. L., 2016, "*On the effects of turbulence modeling on the fluid-structure interaction of a rigid cylinder*," Proceedings of the ASME 2016 35th, International Conference on Ocean, Offshore and Artic Engineering, Busan, South Korea, June 19-24. (OMAE2016-54989)

[22] An, H., Cheng, L. Zhao, M., Tong, F., 2016, "*Numerical simulations of flow around a circular cylinder at high Reynolds number*," Falata editorial (Ed.), Proceedings of the 12th Pacific-Asia Offshore Mechanics Symposium Gold Coast, Australia, October 4-7, pp. 40-46.

[23] Bangga, G., Ashfahani, A., Sugianto, E., Sa'adiyah, D., Putri, T., Jost, E., Lutz, T., 2017, "*Three-dimensional flow in the vicinity of a circular cylinder mounted to a flat plate at high Reynolds number*," AIP Conference Proceedings 1788, Paper No. 030012.

[24] Ong, M. C., Trygsland, E., Myrhaug, D., 2017, "*Numerical study of seabed boundary layer flow around monopile and gravity-based wind turbine foundations*," Journal of Offshore Mechanics and Arctic Engineering 139, Paper No. 042001.

[25] Menter, F. R., 1993, "*Zonal two equation k-ω turbulence models for aerodynamic flows*," 24th Fluid Dynamics Conference, Orlando, Florida, July 6-9. (AIAA Paper No. 93-2906)

ISSN 2448-5837

Edición digital

[26] Menter, F. R., 1994, "*Two-equation eddy-viscosity turbulence models for engineering applications*". American Institute of Aeronautics and Astronautics Journal 32(8), pp. 1598-1605.

[27] Wilcox, D. C., 1998, *Turbulence Modeling for CFD*, 2nd ed. DCW Ind., Inc., La Canada, CA.

[28] Jones, W. P., Launder, B.E., 1973, "*The calculation of low-Reynolds-number pheomena with a two-equation model of turbulence*," International Journal of Heat and Mass Transfer 16(6), pp. 1119-1130.

[29] "*Na Kika Host Facility, Fact Sheet, BP*.," last modified June 14, 2013, http://www.bp.com/content/dam/bp-country/en_us/PDF/Na_Kika_Fact_Sheet_6_14_2013.pdf

[30] "*International Towing Tank Conference, Fresh water and seawater properties*," ITTC-Recommended. Procedures 2011, last modified September, 2011, https://ittc.info/media/4048/75-02-01-03.pdf.

[31] Delany, N. K., and Sorensen, N. E., 1953, "*Low-speed drag of cylinders of various shapes*," National Advisory Committee for Aeronautics, Technical Note 3038.

[32] Pang, A. L. J., Skote, M., Lim, S. Y., 2016, "*Modelling high Re flow around a 2D cylindrical bluff body using the k-ω (SST) turbulence model*," Progress in Computational Fluid Dynamics 16(1), pp. 48-57.

[33] Tanaka, N., Ikeda, Y. and Nishino, K., 1983, "*Hydrodynamic viscous force acting on oscillating cylinders with various shapes*," Osaka University, Department of Naval Architecture, Report No. 407, 6th Symposium of Marine Technology of the Society of Naval Architects of Japan, 1982.

Edición digital

ISSN 2448-5837